INSTITUTE OF PHYSICS PUBLISHING PHYSICS IN MEDICINE AND BIOLOGY

Phys. Med. Biol. **52** (2007) 141–168 doi:10.1088/0031-9155/52/1/010

Quantitative spatially resolved measurement of tissue chromophore concentrations using photoacoustic spectroscopy: application to the measurement of blood oxygenation and haemoglobin concentration

Jan Laufer, Dave Delpy, Clare Elwell and Paul Beard

Department of Medical Physics & Bioengineering, University College London, Malet Place Engineering Building, London WC1E 6BT, UK

Received 8 August 2006, in final form 27 October 2006
Published 14 December 2006
Online at stacks.iop.org/PMB/52/141

Abstract

A new approach based on pulsed photoacoustic spectroscopy for non-invasively quantifying tissue chromophore concentrations with high spatial resolution has been developed. The technique is applicable to the quantification of tissue chromophores such as oxyhaemoglobin (HbO_2) and deoxyhaemoglobin (HHb) for the measurement of physiological parameters such as blood oxygen saturation (SO_2) and total haemoglobin concentration. It can also be used to quantify the local accumulation of targeted contrast agents used in photoacoustic molecular imaging. The technique employs a model-based inversion scheme to recover the chromophore concentrations from photoacoustic measurements. This comprises a numerical forward model of the detected time-dependent photoacoustic signal that incorporates a multiwavelength diffusion-based finite element light propagation model to describe the light transport and a time-domain acoustic model to describe the generation, propagation and detection of the photoacoustic wave. The forward model is then inverted by iteratively fitting it to measurements of photoacoustic signals acquired at different wavelengths to recover the chromophore concentrations. To validate this approach, photoacoustic signals were generated in a tissue phantom using nanosecond laser pulses between 740 nm and 1040 nm. The tissue phantom comprised a suspension of intralipid, blood and a near-infrared dye in which three tubes were immersed. Blood at physiological haemoglobin concentrations and oxygen saturation levels ranging from 2% to 100% was circulated through the tubes. The signal amplitude from different temporal sections of the detected photoacoustic waveforms was plotted as a function of wavelength and the forward model fitted to these data to recover the concentrations of HbO_2 and HHb, total haemoglobin concentration and SO_2. The performance was found to compare favourably to that of a laboratory CO-oximeter with measurement resolutions of $\pm 3.8\ g\,l^{-1}$ ($\pm 58\ \mu M$)

and ± 4.4 g l^{-1} (± 68 μM) for the HbO_2 and HHb concentrations respectively and $\pm 4\%$ for SO_2 with an accuracy in the latter in the range -6%–$+7\%$.

1. Introduction

Biomedical photoacoustic imaging is based upon the generation of broadband (tens of MHz) ultrasound waves by the absorption of nanosecond pulses of visible or near-infrared (NIR) laser light in soft tissue structures such as blood vessels. By measuring the time of arrival of the acoustic waves over the tissue surface, and knowing the speed of sound in tissue, the acoustic signals can be spatially resolved and back projected to form a 3D image of the internally absorbed laser energy distribution which in turn is a function of the distribution of the tissue optical properties. The fundamental advantage of the technique is that, by encoding the distribution of tissue optical properties on to acoustic waves in this way, it overcomes the spatial resolution limitations of purely optical imaging methods (such as diffuse optical tomography) that arise due to the overwhelming optical scatter in soft tissues. As a consequence it can be regarded as hybrid imaging modality that provides the high contrast and specificity of optical techniques along with the high spatial resolution of ultrasound. The latter is depth dependent being limited by the frequency-dependent nature of acoustic attenuation in tissue—for cm penetration depths, sub-mm spatial resolution is possible, decreasing to sub-100 μm for mm penetration depths and sub-10 μm spatial resolution for depths of a few hundred microns. The most important source of naturally occurring contrast for photoacoustic imaging is haemoglobin on account of its strong optical absorption. This makes the technique particularly well suited to imaging blood vessels (Kolkman *et al* 2003, Niederhauser *et al* 2005, Zhang and Beard 2006) and thus the clinical diagnosis and monitoring of tissue pathologies characterized by structural changes in the vasculature such as tumours in the breast (Oraevsky *et al* 2002), or skin (Oh *et al* 2006). In addition to clinical applications, photoacoustic imaging has strong potential as a research tool for imaging small animal models of human disease processes (Wang *et al* 2003, Kruger *et al* 2003).

As well as providing high resolution anatomical information, there is the potential to provide spatially resolved quantitative physiological and molecular information by exploiting the known spectral characteristics of specific chromophores. For example, by obtaining images at multiple wavelengths it is, in principle, possible to quantify the local concentrations of spectrally distinct endogenous chromophores such as oxyhaemoglobin (HbO_2) and deoxyhaemoglobin (HHb) for the calculation of absolute blood oxygen saturation (SO_2). This offers the prospect of obtaining high resolution 3D maps of the distribution of SO_2 over the vasculature for studying oxygen heterogeneity in tumours and other tissue pathologies characterized by abnormalities in tissue oxygenation or perfusion. A further important spectroscopic application is the detection and quantification of exogenous chromophores such as those used in photoacoustic molecular imaging (Kruger *et al* 2003, Xie *et al* 2006). Here a spectrally distinct chromophore is tagged to a systemically introduced molecular probe designed to bind to a disease-specific receptor such as a cell-surface protein or enzyme. Using spectroscopic methods to quantify the local accumulation of the molecular probe, and thus the expression levels of disease-specific proteins or genes, offers the prospect of eliciting the molecular basis of disease processes, not solely their anatomical and physiological manifestations.

Ultimately, the goal of *in vivo* quantitative spectroscopic photoacoustic imaging is to provide maps of the absolute concentration of chromophores (both endogenous and exogenous)

distributed throughout the tissue. However, if this ambitious objective is to be realized, a rigorous and experimentally validated methodology is required. The first step in this endeavour, and the objective of this paper, is to develop methods that relate the fundamental measured spectroscopic quantity, the wavelength-dependent time-resolved photoacoustic signal, to the spectral characteristics of the chromophores and scatterers that make up the tissue.

Previous efforts have been largely directed towards studying photoacoustic spectra in blood with a view to quantifying HbO_2 and HHb concentrations and various derived parameters, such as SO_2 and total haemoglobin concentration. Initial investigations were limited to generating photoacoustic signals in a cuvette filled with blood—i.e., a homogeneous target. The earliest studies of this nature demonstrated that the wavelength dependence of specific characteristics of the photoacoustic signals generated are in qualitative agreement with the known SO_2-dependent absorption spectrum of blood but fell short of recovering either absolute HbO_2 and HHb concentrations or SO_2 from the measurements (Fainchtein *et al* 2000, Savateeva *et al* 2002, Esenaliev *et al* 2002). This was redressed in a subsequent study in which experimentally validated photoacoustic measurements of absolute blood SO_2 were made using linear (Laufer *et al* 2004) and nonlinear (Laufer *et al* 2005) model-based inversion methods. The latter comprised a forward model of the wavelength-dependent photoacoustic signal, based upon an analytical solution of the diffusion equation, which was inverted to yield HHb and HbO_2, and thence SO_2 by fitting it to measured photoacoustic spectra. This showed that SO_2 could be estimated to an accuracy of $\pm 2.5\%$ and a resolution of $<1\%$, a performance that is comparable to that of a commercial laboratory CO-oximeter.

Cuvette-type measurements of this type are valuable as a first step as they demonstrate the quantitative ability of photoacoustic spectroscopy. They are however of limited broader applicability as the inversion algorithms are valid only for an optically homogeneous target. They do not therefore demonstrate the fundamental distinguishing advantage of the technique which is its ability to provide *spatially resolved* information. Here, the critical issue is accounting for the wavelength dependence of the light distribution surrounding the region of interest. For example, the wavelength dependence of the photoacoustic signal emitted by a discrete blood vessel will be encoded not only with the absorption spectra of the HHb and HbO_2 within the vessel but also the spectral characteristics of the chromophores and scatterers in the illuminated region surrounding it—the HHb and HbO_2 in the surrounding capillary bed, water and lipids in the extravascular space and melanin in the skin can all provide a significant spectral contribution. Early studies in heterogeneous media (Paltauf *et al* 2001, Wang *et al* 2004) did not account for this, employing a simple linear spectroscopic decomposition (such as that used in conventional optical spectroscopy) which assumes the photoacoustic spectrum corresponding to a specific point is related solely to the absorption spectra of the chromophores at that point. Given the methodological limitations and the absence of experimental validation studies either *in vivo* or in tissue phantoms, spatially resolved quantitative *in vivo* measurements using this approach are likely to be, at best, of indeterminate accuracy.

Subsequent studies have acknowledged the need to address this issue (Maslov *et al* 2006, Stantz *et al* 2006, Wang *et al* 2006, Laufer *et al* 2006a, 2006b). One approach is to modify the above type of linear spectroscopic decomposition by incorporating empirical correction or calibration factors that account for the wavelength dependence of the external light distribution. For example, it has been suggested that the spectral characteristics of the tissue overlaying the region of interest could be accounted for by measuring the light transmission as a function of wavelength through a sample of excised tissue of the same type (Wang *et al* 2006). Another proposed method of obtaining the same type of information involved measuring the photoacoustic spectrum of a black plastic absorber (of presumably uniform or known spectral characteristics) embedded beneath the skin of a live mouse at the

depth of interest (Maslov *et al* 2006). The drawback with such empirical correction factors, apart from the invasive methods required to obtain them, is that they are highly dependent upon the tissue structure, composition and physiology (particularly perfusion and oxygenation status). Given that these vary significantly between different tissue types and over time, this inevitably limits their general applicability.

A fundamentally different approach, and one that has the potential to avoid these limitations, is to account for the wavelength-dependent light distribution, not by using empirical correction factors, but through an explicit mathematical representation within the forward model. This is the approach described in this paper—the light distribution being represented by a diffusion-based finite element (FE) model of light propagation. Because the latter can be formulated as a function of an arbitrary spatial distribution of any number of chromophores, this approach is applicable, in principle, to any tissue geometry or type. Furthermore, it offers a high degree of confidence in its use, not only because it explicitly accounts for the relevant physical mechanisms underlying the generation of photoacoustic spectra but because it can be rigorously and systematically validated using tissue mimicking phantoms.

Preliminary details of this approach have been described in Laufer *et al* (2006a, 2006b), which include the first experimentally validated spatially resolved measurements of absolute blood SO_2. In this paper we provide a comprehensive account of the methodology, both the forward model (section 3) and the inversion scheme (section 4) and its application to the recovery of absolute chromophore concentrations in a spatially and spectrally heterogeneous tissue phantom. Section 5 describes the tissue phantom and the experimental technique used to obtain the measured spectroscopic photoacoustic data. Section 6 discusses the accuracy of the chromophore concentrations and other parameters recovered from these measurements and the associated sources of error.

2. Model-based inversion scheme: overview

This paper describes a model-based inversion scheme for recovering the absolute concentrations of specific chromophores distributed throughout a tissue sample from a set of measured time-resolved photoacoustic signals generated at multiple wavelengths. By 'model based' it is meant that a mathematical forward model is formulated that describes the physical processes involved in the generation of the photoacoustic signals. The model is then inverted to recover a specific parameter set, in this case the absolute values of the concentrations of the tissue chromophores, from the measured data. There are two critical and challenging aspects to this inverse problem. First, an accurate forward model that properly accounts for all the physical mechanisms is required. Thus the wavelength-dependent light transport in tissue must be incorporated, in itself nontrivial given the highly scattering nature of soft tissues, as must the subsequent generation and propagation of the acoustic wave along with its interaction with the detection instrumentation. Given the multi-parameter nature of the problem, the second critical aspect is to ensure the existence of a unique solution to the inverse problem by limiting the number of unknowns. Our hypothesis is that this is achievable by assuming that the number of chromophores and scatterers that exist in tissue, and their spectral characteristics, are known *a priori*. With this prior information only, and an accurate forward model of the photoacoustic signal generation process, it should then be possible to make measurements of chromophore concentrations that are both quantitative and spatially resolved.

In order to develop and experimentally test this methodology, a specific target geometry was studied. This was designed to meet three requirements. First, it should contain a

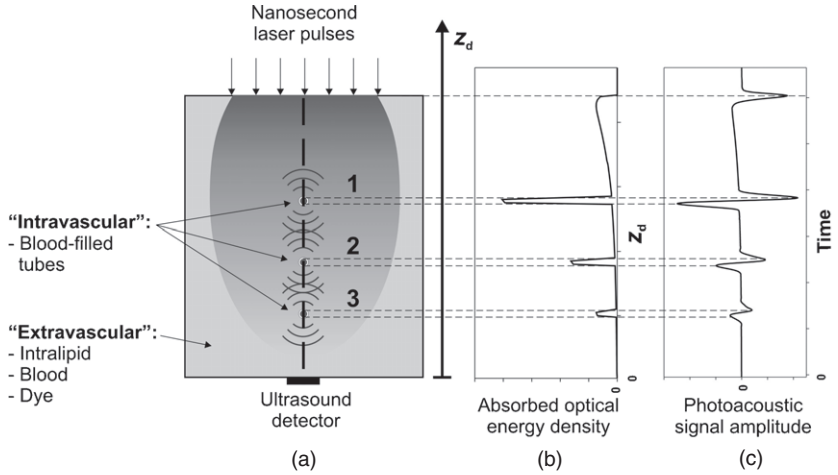

Figure 1. (a) Tissue phantom design, (b) depth profile of the absorbed optical energy along the vertical line of sight of the ultrasound transducer (the dashed line in the z_d direction). (c) A schematic of the photoacoustic waveform detected by the ultrasound receiver.

sufficient number of spectrally distinct chromophores with sufficient spatial heterogeneity to demonstrate the generality of the technique. Second, the number, type and spatial distribution of the constituent chromophores should be broadly representative of biological tissue. Third, it can be accurately and repeatedly reproduced in the laboratory. With these requirements in mind the tissue phantom design shown in figure 1 was employed. The specific experimental details of the phantom are given in section 5.2. Briefly, it comprises three discrete blood perfused tubes, termed the 'intravascular space', designed to represent a simple vascular network. The tubes are immersed in a homogeneous turbid liquid, an aqueous solution of intralipid, termed the 'extravascular space'. As well as simulating the strong optical scattering exhibited by soft tissues, this solution provides two key NIR background tissue chromophores: water and lipids. Additionally, it contains a small amount of blood in order to represent the background absorption due to the capillary bed. A near-infrared dye representing a notional externally administered contrast agent was also added to the extravascular space to provide an additional chromophore. Thus the phantom contains a total of four spatially distributed 'endogenous' tissue chromophores, HbO_2 and HHb, water and lipid and one 'exogenous' chromophore, the near-infrared dye. The task is to quantify the concentrations of each of these chromophores with specific emphasis on recovering the intravascular concentrations of HbO_2 and HHb. These are of particular significance as they enable the physiologically important parameters, the blood oxygen saturation SO_2 and total haemoglobin concentration, to be determined.

Photoacoustic signals are generated in the phantom by irradiating the surface with nanosecond pulses of NIR laser light. The absorption of the optical energy leads to near impulsive heating of the irradiated volume followed by rapid thermoelastic expansion. This produces an initial stress distribution, proportional to the absorbed optical energy distribution, which is encoded on to a broadband ultrasonic thermoelastic wave that propagates to an ultrasound receiver positioned on the opposite side to the irradiated surface. This process is illustrated schematically in figures 1(b) and (c). Figure 1(b) shows the absorbed optical energy as a function of z_d. It is characterized by three peaks, one for each blood-filled tube. The relatively large amplitude of the peaks is due to the strong preferential optical

absorption exhibited by the haemoglobin within the tubes. These peaks are superimposed on the z_d-dependent absorbed energy profile within the more weakly absorbing turbid liquid in the extravascular space. This increases gradually from $z_d = 0$, approximately exponentially where the light is fully diffuse, rising to a maximum at, or close to, the surface. Assuming the detector is essentially directional and receives signals predominantly only along its vertical line of sight, the detected time-resolved photoacoustic signal (figure 1(c)) is given, to a first approximation, by taking the spatial derivative of the absorbed energy distribution and converting distance to time using the speed of sound. The detected signal therefore comprises a series of discrete bipolar pulses, one for each tube and one for the surface, superimposed on the weaker, slowly varying background signal originating from the extravascular space. In this way, the time record of the detected photoacoustic signal provides a direct representation of the depth profile of the absorbed energy within the target.

By capturing photoacoustic signals at different excitation wavelengths and plotting the amplitude for each point in the time record of the signals as a function of wavelength, a set of absorbed optical energy spectra, each corresponding to a specific depth, can be obtained. The question is what these spatially resolved spectra represent. Specifically, what is the relationship between the absorbed energy spectrum at a specific point and the composite absorption spectrum of the ensemble of chromophores at that point? At first sight, it might appear that the former is proportional to the linear sum of the absorption spectra of all the chromophores at the spatial point in question. This would allow a simple linear spectroscopic decomposition, such as the type used in conventional transmission optical tissue spectroscopy (Wray *et al* 1988, Cope 1991), to be used to recover the concentrations of each chromophore. However, this would imply that the time-resolved photoacoustic signal amplitude is proportional to the local absorption coefficient alone. This is clearly not the case. The signal amplitude is proportional to the absorbed energy and this is the product of the local absorption coefficient and the fluence, the latter being a function of the distribution of absorption and scattering coefficients over the entire illuminated tissue volume. The spectral characteristics of all the different chromophores and scatterers distributed throughout this volume will therefore, to some extent, be encoded on to the measured absorbed energy spectrum at a specific point. An obvious example of this occurs when two spectrally distinct absorbers are located such that one lies directly beneath the other. Since the light will have passed through the top absorber to reach the one beneath it, the absorbed energy spectrum of the latter will be composed of the spectral characteristics of both. Indeed given that in tissue, a photon can be scattered from one point to any other, this type of spectroscopic crosstalk can occur even if two absorbers are located side by side at the same depth or indeed, if there is significant backscattering, from a deeply lying absorber to another situated directly above it. As a consequence, it is unlikely that a standard linear spectroscopic decomposition will provide quantitatively accurate chromophore concentrations for anything other than a few limited cases, for example a homogeneous target (Laufer *et al* 2005) as discussed in the appendix. If spectroscopic photoacoustic methods are to be successful in providing accurate quantitative information in geometrically and spectrally heterogeneous media such as biological tissue, a more sophisticated model-based inversion approach that explicitly accounts for the wavelength-dependent light distribution over the whole illuminated tissue volume is required. It is this approach that forms the basis of the methodology described in this paper.

The practical realization of this approach involves formulating a forward model that can generate theoretical photoacoustic signals at multiple wavelengths for an arbitrary spatial distribution of chromophore concentrations, the model input parameters. The forward model is then inverted by iteratively adjusting its input parameters until it fits the measured spectroscopic photoacoustic signals to yield the true chromophore concentrations. The key components of

this scheme, the forward model and the inversion scheme, are described in sections 3 and 4, respectively.

3. The forward model

The essential requirement of the forward model is that it can predict the wavelength-dependent photoacoustic waveforms as a function of the spatial distribution of chromophore concentrations. To achieve this, a model of the detected time-dependent photoacoustic signal as a function of the spatial distribution of the absorption and scattering coefficients is initially formulated for a single optical wavelength. This was realized using a diffusion-based finite element (FE) light transport model to provide the initial absorbed optical energy distribution (section 3.1). From this the initial pressure distribution is obtained and the subsequent generation, propagation and detection of the photoacoustic wave computed using a time-domain acoustic model (section 3.2) to yield the detected photoacoustic signal. To obtain the complete multiwavelength forward model, the absorption coefficients in the single wavelength model are then expressed in terms of the concentrations and specific extinction spectra of the constituent chromophores and the scattering coefficients in terms of the wavelength dependence of the scatterers (section 3.3).

3.1. The absorbed optical energy distribution

To describe the absorbed optical energy density distribution, Q, due to the incident pulsed laser irradiation, a model of light transport is required. The essential requirements of the model are that it can accurately represent the highly scattering nature of light transport in tissue, be formulated as a function of arbitrary spatial distributions of absorption and scattering coefficients and is computationally efficient enough to be used iteratively within the proposed inversion scheme. To meet these requirements, a 2D FE implementation of the time-independent diffusion approximation to the radiative transport equation is used (Cox *et al* 2006b). To ensure that the light transport is modelled accurately close to the irradiated surface, where the light retains its directionality and is not near isotropic as is required for the standard diffusion approximation, a simple adjustment to the scattering parameters based upon consideration of the delta-Eddington phase function is employed (Laufer *et al* 2005, Cox *et al* 2006a).

The FE model is general in the sense that it can account for arbitrary distributions of optical coefficients. However, to minimize runtime when using the model iteratively, the *general* spatial characteristics of the target shown in figure 1(a) are incorporated *a priori*. That is to say, it is assumed that the target consists of an optically homogeneous extravascular space containing any number of discrete absorbers of arbitrary dimensions distributed arbitrarily along the line of sight of the detector. Note that this is the only prior geometric information incorporated. Although the specific number, dimensions and positions of the discrete absorbers are also entered into the model, they are not regarded as prior knowledge as they are recovered from the temporal positions and widths of the peaks in the measured time-dependent photoacoustic signal (figure 1(b)).

The 2D absorbed energy distribution Q for a collimated incident beam with a top hat intensity profile and of diameter d_b is written as

$$Q(x, z, \mu_a(x, z), \mu_s, g, d_b) = \mu_a(x, z)\Phi_0\Phi(x, z, \mu_a(x, z), \mu_s, g, d_b), \qquad (1)$$

where x is the horizontal distance and z is the vertical distance from the illuminated surface. Φ is the internal fluence distribution normalized to that at the surface, Φ_0. μ_a and μ_s are

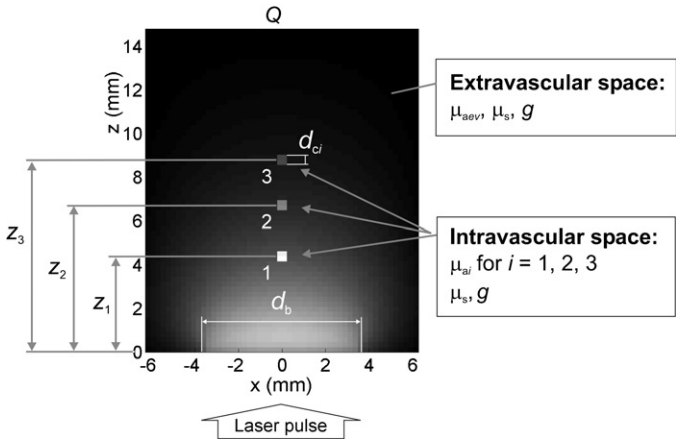

Figure 2. An example of the output of the 2D FE light transport model showing the absorbed energy density distribution, Q, for the geometry of figure 1(a). The grid element size is 230 μm.

the absorption and scattering coefficients respectively and g is the anisotropy factor. To incorporate the general spatial characteristics of the target shown in figure 1(a) in the model, $\mu_a(x, z)$ is defined for the intravascular and extravascular space (as shown in the example of the model output in figure 2) thus,

$$\mu_a(x,z) = \begin{cases} \mu_{ai} & \text{for } 0 - \dfrac{d_{ci}}{2} \leqslant x \leqslant 0 + \dfrac{d_{ci}}{2} \text{ and } z_i - \dfrac{d_{ci}}{2} \leqslant z \leqslant z_i + \dfrac{d_{ci}}{2} \\ \mu_{aev} & \text{elsewhere} \end{cases} \right\}$$
$$i = 1, 2, 3 \ldots N, \tag{2}$$

where the absorption within the intravascular space is defined by μ_{ai}, d_{ci} and z_i, the absorption coefficient, diameter and z position respectively of the ith tube lying along the detector line of sight (the line $x = 0$). N is the total number of tubes, so for the geometry of figure 1(a), $N = 3$. The absorption coefficient in the homogeneous extravascular space is given by μ_{aev}. Although the scattering parameters μ_s and g can be defined similarly, they were set to be the same throughout the domain given the near-homogeneous scattering distribution in the tissue phantom used.

An example of the output of the model for three discrete absorbers within a homogeneous background is provided in figure 2 for a 12.5 mm $\times$ 14.8 mm domain with a grid element size of 230 μm. This shows the lateral spreading and gradual decrease in the absorbed energy with z in the extravascular space and the relatively higher absorbed energy in the tubes as illustrated schematically in the depth profile in figure 1(b).

The task now is to compute the initial pressure distribution from Q and the subsequent propagation and detection of the acoustic wave. This is described in the following section.

3.2. Acoustic generation, propagation and detection

Given the absorbed optical energy distribution, Q, as described in the previous section, there are three remaining physical processes to be accounted for in order to model the photoacoustic signal recorded by the detector: first, the conversion of the absorbed optical energy distribution to the initial pressure distribution, p_0; second, the propagation of acoustic wave energy from p_0 and third, the interaction of the acoustic wave with the detector.

Assuming the laser pulse duration is sufficiently short to ensure thermal and stress confinement (Cox and Beard 2005), the initial pressure distribution p_0 is proportional to the absorbed optical energy distribution Q thus,

$$p_0(x, z, \mu_a(x, z), \mu_s, g, d_b) = \Gamma Q(x, z, \mu_a(x, z), \mu_s, g, d_b), \tag{3}$$

where Γ is the Grüneisen coefficient, a measure of the efficiency of the conversion of heat energy to stress. The subsequent propagation of the acoustic wave is then given by solving the 3D acoustic wave equation with p_0 providing either the source term for the inhomogeneous wave equation or the initial conditions for the solution of the homogeneous equation (Cox and Beard 2005). One commonly used numerical time-domain propagation model is based on Poisson's integral solution of the wave equation for an acoustically linear isotropic homogeneous and non-absorbing medium (Landau and Lifshitz 1987, Paltauf *et al* 1996, Köstli and Beard 2003). This is given by

$$p(r, t) = \frac{1}{4\pi c}\frac{\partial}{\partial t}\int_{|\Delta r|=ct} \frac{p_0(r - \Delta r)}{ct}\, \mathrm{d}s. \tag{4}$$

Equation (4) states that the time-integrated acoustic pressure, or velocity potential, at a detector position $\mathbf{r}$ and time t is equal to the sum of all points in the initial pressure distribution that lie on a spherical surface s centred on $\mathbf{r}$ and of radius Δr equal to the product of the speed of sound c and t. Evaluating equation (4) as a function of t provides the time record of the photoacoustic signal $p(t)$ as measured by an ideal point detector. To account for a more realistic detector (i.e., one of finite size) it is necessary to spatially average the incident acoustic wave over the sensitive volume of the detector. This is most efficiently implemented by invoking the principle of acoustic reciprocity and convolving p_0 with the detector geometry as described in Köstli and Beard (2003). Equation (4) is then evaluated with the convolved initial pressure distribution p_0^* in place of p_0. Although efficient enough for non-intensive use, for example as an occasional simulation tool, this model is too computationally expensive for iterative use as required in the proposed inversion scheme. For this reason, it was implemented in an approximate, but more efficient, manner by circumventing its two most computationally demanding aspects, the source-detector spatial convolution and the requirement for a 3D domain.

The source-detector convolution represents the greatest computational burden. It was avoided by assuming its spatial averaging effect can be equivalently decomposed into the detector frequency response and directivity, and then accounting for each individually. The frequency response (for normal incidence) is defined by the detector thickness and can be neglected if the latter is small compared to the dimensions of the source geometry. This is reasonable in this study as the spatial scales of the detector and source geometries typically differ by an order of magnitude. By contrast, the directivity is defined by the diameter of the detector. This is required to be large compared to the source dimensions to provide the necessary directional response and cannot therefore be neglected. To incorporate the directivity, equation (4) (evaluated with p_0^* in the integral) was used to simulate the detector output in response to a signal emitted by a point source as a function of position. This provided a 2D relative sensitivity map $D(x, z)$ that delineates the region over which a source must be located for its output to be registered by the detector. The sensitivity map was then imposed directly on the initial pressure distribution by computing the product of $D(x, z)$ and p_0. In this way, the finite lateral size of the receiver, and therefore its directional characteristics are incorporated through a multiplicative operation rather than the more computationally expensive spatial convolution.

The second approximation involves explicitly incorporating the attenuation due to the geometric spreading of the propagating acoustic wavefront. Although this is implicit in

equation (4), it requires evaluating the integral in 3D. As with the source-detector convolution, this involves significant computational overhead if performed iteratively. To avoid this, the attenuation was computed for the specific source geometries in the target using equation (4), again with p_0^* in the integral, to form a 2D attenuation map $A(x, z)$—for the wavefronts emitted by the tubes (for the dimensions used in this study), the attenuation was found to be proportional to z_d^{-1} and for the extravascular space at the surface, a weaker $z_d^{-2/3}$ dependence was obtained. The attenuation map was then imposed directly on the initial pressure distribution by taking the product of $A(x, z)$ and p_0.

In summary, obtaining the detected time-dependent photoacoustic waveform $p(t)$ requires three steps: (1) the absorbed energy distribution Q is computed using the FE light transport model described in section 3.1. (2) p_0 is then calculated from Q using equation (3) and modified by multiplying by $D(x, z)$ and $A(x, z)$ and (3) the modified p_0 is then substituted into equation (4) which is then evaluated in 2D (with the denominator set to a constant) to yield the acoustic pressure $p(t)$ as a function of time. Note that evaluating equation (4) in 2D required performing the integration over the circumference of a circle rather than a spherical surface.

Finally, $p(t)$ is multiplied by the system response constant, K, which depends on the detector sensitivity to yield the measured signal $S(t)$,

$$S(t) = Kp(t, \mu_a(r), \mu_s(r)). \tag{5}$$

Equation (5) represents the forward model of the time-resolved photoacoustic signal amplitude as a function of the spatial distribution of the optical coefficients.

3.3. Incorporating the wavelength dependence of the constituent chromophores and scatterers

The final step in the formulation of the forward model is the inclusion of the wavelength dependence of the constituent chromophores and scatterers by writing μ_a and μ_s in equation (5) in terms of their spectral characteristics. This enables the wavelength dependence of the photoacoustic amplitude for each point in the time record of the signal to be computed.

Up to this point the only prior information incorporated in the forward model has been the non-specific spatial characteristics of the target as described in section 3.1. Now, to ensure a unique solution when the model is inverted, it is necessary to incorporate the following specific prior information: the number, type and specific absorption spectra of the chromophores within the target and the wavelength dependence of the scattering. This represents the central premise behind the approach outlined in this paper: that tissue is made up of a known number of spectrally significant constituents (water, lipid, haemoglobin etc) whose spectral characteristics are also known, but whose abundance is not.

In the phantom depicted in figure 1(a) there are a total of five chromophores distributed throughout the target: HbO_2, HHb, water, lipid and a near-infrared dye (ADS780WS, American Dye Source Inc.). The absorption coefficient spectra for each of these are shown in figure 3. To incorporate these spectral characteristics in the forward model, $\mu_a(\lambda)$ in equation (5) is expressed as the linear sum of the products of the concentration and the specific absorption coefficient for each chromophore in the intravascular and extravascular space as follows.

The intravascular space comprises the three blood-filled tubes and is assumed to be composed of HbO_2, HHb and water. Thus, using the nomenclature of equation (2), the absorption coefficient for the ith tube is written as

$$\mu_{ai}(\lambda) = \alpha_{HHb}(\lambda)c_{HHbi} + \alpha_{HbO_2}(\lambda)c_{HbO_2 i} + \alpha_{H_2O}(\lambda)c_{H_2Oi} \qquad \text{for } i = 1, 2, 3 \tag{6}$$

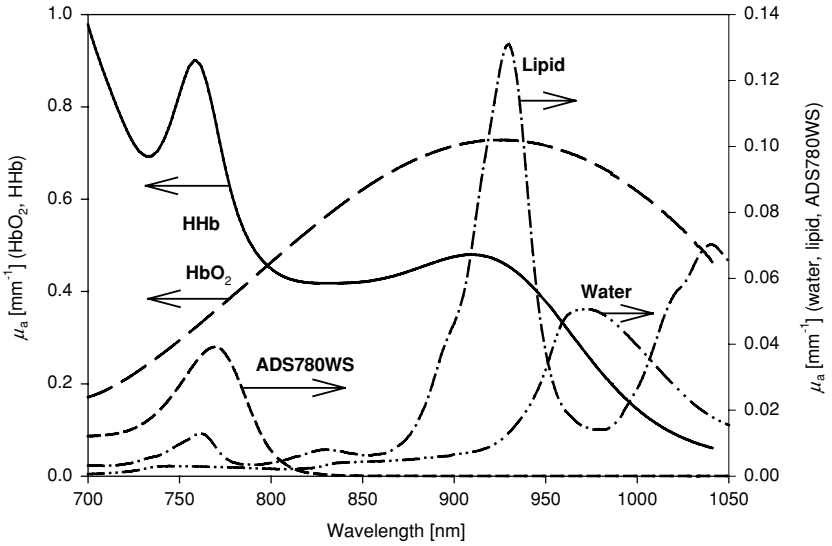

Figure 3. Near-infrared absorption coefficient spectra of the chromophores present in the tissue phantom shown in figure 1(a): oxyhaemoglobin (HbO_2) and deoxyhaemoglobin (HHb) ($c_{HbO_2} = c_{HHb} = 150$ g l^{-1}), water, lipid and a near-infrared dye (ADS780WS, $c_{Dye} = 2\ \mu$M).

where $\alpha_{HHb}(\lambda)$, $\alpha_{HbO_2}(\lambda)$ and $\alpha_{H_2O}(\lambda)$ are the wavelength-dependent specific absorption coefficients (units: mm^{-1} M^{-1}, defined using the natural log) of HHb, HbO_2, and water respectively and c_{HHbi}, $c_{HbO_2 i}$, and c_{H_2Oi} are the corresponding intravascular concentrations of these chromophores. The specific absorption spectra were obtained from published data with $\alpha_{HbO_2}(\lambda)$ and $\alpha_{HHb}(\lambda)$ from Cope (1991) and $\alpha_{H_2O}(\lambda)$ from Hale and Querry (1973).

The extravascular space, the intralipid solution, also contains HbO_2, HHb and water plus a further two chromophores, lipid and the near-infrared dye. The absorption coefficient μ_{aev} for this region is therefore written

$$\mu_{aev}(\lambda) = \alpha_{HHb}(\lambda)c_{HHbev} + \alpha_{HbO_2}(\lambda)c_{HbO_2ev} \ldots + \alpha_{Dye}(\lambda)c_{Dye} + \alpha_{Lipid}(\lambda)c_{Lipid} + \alpha_{H_2O}(\lambda)c_{H_2Oev}, \quad (7)$$

where $\alpha_{Dye}(\lambda)$ and $\alpha_{Lipid}(\lambda)$ are the wavelength-dependent specific absorption coefficients of the near-infrared dye and lipid, respectively. $\alpha_{Lipid}(\lambda)$ was based on measurements by van Veen *et al* (2005), while $\alpha_{Dye}(\lambda)$ was provided by the manufacturer of the dye. c_{HHbev}, c_{HbO_2ev}, c_{Dye}, c_{Lipid}, c_{H_2Oev} are the chromophore concentrations, the subscript '*ev*' denoting the extravascular space.

As described in section 3.1, the scattering coefficient is assumed to be the same for the intravascular and extravascular space, and is given by

$$\mu_s(\lambda) = \alpha_{scat}(\lambda)k_{scat}, \quad (8)$$

where $\alpha_{scat}(\lambda)$ is the scattering efficiency, which represents the normalized wavelength dependence of the scattering dependence, and k_{scat} is a scaling factor that represents the strength of the scattering and is dependent upon parameters such as the size and concentration of the scatterers. $\alpha_{scat}(\lambda)$ was obtained from μ_s spectra measured in intralipid (van Staveren *et al* 1991).

Equations (6), (7) and (8) can now be used to express $\mu_a(\lambda)$ and $\mu_s(\lambda)$ in equation (5) in terms of their wavelength dependence to yield the complete multiwavelength forward model.

4. Numerical inversion scheme

The previous section has shown how a forward model that can generate wavelength-dependent time-resolved photoacoustic signals as a function of chromophore concentrations can be formulated. Given a set of measured time-resolved photoacoustic signals at different wavelengths, the task now is to invert the forward model. That is to say, find the set of chromophore concentrations that minimize the difference between the model output and measured data. Since the forward model cannot be expressed in closed form, this requires a numerical inversion scheme whereby the output of the model is iteratively fitted to the measurements.

First the model input parameter set is defined. These are divided into the following known and unknown parameters:

Known fixed input parameters:

$\{\alpha_{HHb}(\lambda), \alpha_{HbO_2}(\lambda), \alpha_{Dye}(\lambda), \alpha_{Lipid}(\lambda), \alpha_{H_2O}(\lambda), \alpha_{scat}(\lambda), g, c_{H_2Oi}, c_{H_2Oev}, c_{Lipid}, d_b, N, d_{ci}, z_i\}$.

Unknown variable parameters:

$\{c_{HHbev}, c_{HbO_2ev}, c_{HHbi}, c_{HbO_2i}, c_{Dye}, k_{scat}, K\}$.

The known input parameters therefore comprise the spectral characteristics of the chromophores and scatterers that make up the tissue and the illumination beam diameter. These are regarded as prior knowledge and entered as fixed input parameters into the model. The geometric parameters relating to the tubes, the number N, position z_i and diameters d_{ci} are also fixed input parameters. However, as outlined in section 3.1, they are not regarded as being known *a priori* since they are recovered from the measured photoacoustic waveform. In addition, the concentrations of intra- and extravascular water and lipids, c_{H_2Oi} and c_{H_2Oev}, respectively, are entered as fixed input parameters. The unknowns, the oxyhaemoglobin and deoxyhaemoglobin and near-infrared dye concentrations, the scattering and system response scaling factors, k_{scat} and K, are the adjustable input parameters of the model.

To recover the chromophore concentrations requires the following steps. First, the measured data, a set of time-dependent photoacoustic signals at different wavelengths, are acquired. In other words, the complete measured data set comprises a set of photoacoustic spectra, one spectrum for each point in the time record of the photoacoustic signal. The inversion then seeks to recover the concentrations by fitting the forward model to all of these measured photoacoustic spectra simultaneously—in principle it can be fitted to each measured data point in time and wavelength space although in practice the signal amplitude was extracted at discrete temporal positions in the photoacoustic waveform (as described in section 5.3) to limit the size of the measured data set.

The fitting procedure involves using the forward model to generate a set of time-dependent photoacoustic signals over the same wavelength range as the measurements for an initial set of chromophore concentrations, the model input parameters. The latter are then iteratively updated (using a simplex-based search) until the sum of the squares of the

differences between theoretical and measured signals is minimized. At this point the values of the chromophore concentrations are regarded to be the 'true' values. The time to execute the inversion scheme was approximately 2 h using a code based on standard interpreted Matlab functions (e.g., fminsearch) executed on a relatively low specification desktop PC (1 GHz processor). Given that the problem scale (in terms of the number of unknowns) is not excessively large, it is envisaged that the use of more efficient gradient-based minimization schemes, compiled code and taking advantage of the higher PC processor speeds (4 GHz) that are now routinely available would enable runtimes of the order of a few minutes to be achieved.

Of particular interest in this study are the concentrations of HbO_2 and HHb and the physiologically important derived parameters, the blood oxygen saturation, SO_2 and total haemoglobin concentration, c_{THb}, given by equations (9) and (10) below:

$$\mathrm{SO}_2[\%] = \frac{c_{\mathrm{HbO}_2}}{c_{\mathrm{THb}}} \times 100 \tag{9}$$

$$c_{\mathrm{THb}} = c_{\mathrm{HHb}} + c_{\mathrm{HbO}_2}. \tag{10}$$

The uncertainty in the determined parameters, u_{p}, was calculated using

$$u_{\mathrm{p}} = \sqrt{\mathrm{var}(P)} = \sqrt{(XX')^{-1}\sigma^2_{\mathrm{p-p}}}, \tag{11}$$

where P is an array of the variable input parameters, var is the variance, X is the design matrix of the model (X' is its conjugate transpose), which contains the derivative of the model with respect to the input parameters, and $\sigma_{\mathrm{p-p}}$ is the standard deviation of the peak-to-peak signal amplitude of the combined spectra, which was obtained from repeated measurements. The values of u_{p} therefore reflect the smallest detectable change, i.e. resolution, in the determined parameters given the error in the measurement.

5. Methods

5.1. Blood preparation

Leucocyte depleted blood samples, which had exceeded the expiry date of 30 days since donation, were obtained from the blood bank of the local hospital. Ethics approval had been granted for this study. 1000 units of heparin were added to 200 ml of blood, which was then centrifuged at 3000 rpm to separate the red blood cells from residual plasma. The plasma was then removed and replaced with a phosphate-buffered saline solution (pH 7.4, Sigma Aldrich). This process was repeated four times to produce a saline suspension of red blood cells. The total intravascular haemoglobin concentration in the phantom was between 120 and 160 g l^{-1} and thus lies within the physiological range.

5.2. Experimental set-up

Figure 4 shows the experimental set-up. The tissue phantom (designed to reproduce the geometry shown in figure 1(a)) comprises a chamber containing intralipid into which three polymethyl methacrylate tubes (460 μm internal diameter, 75 μm wall thickness) were immersed at depths of 4.4, 6.7 and 8.8 mm. A 5 mm thick BK7 glass window forms one side of the chamber to enable the excitation laser pulses to be delivered to the phantom. The intralipid (of lipid concentration 1.5%) had an absorption coefficient of 0.05 mm^{-1} and a reduced scattering coefficient of approximately 1.3 mm^{-1} at 975 nm. These values are similar to those

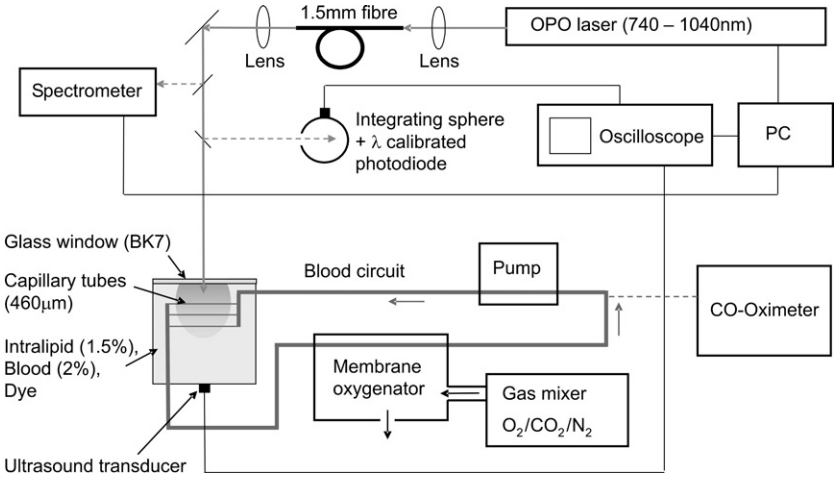

Figure 4. Experimental set-up for measuring spectroscopic photoacoustic signals.

found in biological tissue (Troy *et al* 1996, Simpson *et al* 1997). For certain experiments, a small amount of blood (representing the capillary bed) and a near-infrared dye (ADS780WS) were also added to the intralipid suspension. The total haemoglobin concentration of the blood in the intralipid ranged between 3.7 and 4.1 g l^{-1} and the concentration of the dye was 1.08×10^{-3} g l^{-1}. Sedimentation of the red blood cells was prevented by stirring the intralipid/blood suspension.

The saline suspension of red blood cells was continuously circulated through the tubes and a membrane oxygenator using a peristaltic pump. A gas mixer provided constant flow rates of oxygen, nitrogen and carbon dioxide through the membrane oxygenator. Carbon dioxide flow was held constant at about 5% of the combined flow of nitrogen and oxygen. The blood SO_2 within the tubes was varied from 2% to 100%, by adjusting the ratio of oxygen and nitrogen.

An optical parametric oscillator (OPO) laser system provided 7 ns excitation pulses between 740 nm and 1040 nm at a pulse repetition rate of 10 Hz. The output of the OPO laser was coupled into a fused silica optical fibre (1.5 mm diameter) to homogenize the beam and the output of the fibre was incident on the chamber window. The beam diameter was 7 mm and the incident fluence ranged between 40 and 80 mJ cm^{-2}. The generated photoacoustic waves were detected using an angle-tuned Fabry–Perot ultrasound transducer (Beard *et al* 1999, Beard 2003). Its sensing mechanism is based on the detection of acoustically induced changes in the optical thickness of a 75 μm thick Fabry–Perot polymer film and provides a broadband (15 MHz) detection sensitivity of 0.5 kPa (noise equivalent pressure). A small portion of the incident light was directed to a spectrometer to measure the OPO wavelength with a resolution of 0.3 nm. Another portion of the incident light was directed onto an integrating sphere and measured with a wavelength-calibrated photodiode in order to normalize the photoacoustic waveforms with respect to the incident pulse energy. The photodiode output and the photoacoustic waveforms were captured and averaged over 60 acquisitions using a digital oscilloscope. The acquisition was repeated three times for each wavelength. The wavelength scans were made between 740 nm and 1040 nm in 10 nm steps. The time taken to do a scan was approximately 20 min, although the majority of this was due to the relatively

long download time from the oscilloscope to the PC via the GPIB interface—the OPO itself can scan over its entire wavelength range in less than 10 s.

The linewidth of a type I OPO laser systems is strongly dependent on emission wavelength varying from 2–3 nm FWHM at 1000 nm to 15–25 nm around 740 nm. This results in a smearing of spectral features such as the HHb absorption peak at 760 nm. To account for this, the wavelength-dependent linewidth was measured using a spectrometer and convolved with the known specific absorption spectra of HHb, HbO_2 and the near-infrared dye.

Experiments were undertaken for three different variants of the extravascular space: (1) intralipid, (2) a mixture of intralipid and blood or (3) a mixture of intralipid, blood and the near-infrared dye. In each case, wavelength scans were made for intravascular blood SO_2 levels ranging from 2% to 100%. Small samples of intravascular blood were taken from the circuit at several times before and during the wavelength scan and analysed using a CO-oximeter (IL482, Instrumentation Labs Inc). This provided the total haemoglobin concentration (± 3.0 g l^{-1}) and the haemoglobin fractions $\%HbO_2$ ($\pm 1\%$) and %HHb ($\pm 3\%$). From these, the concentrations of HHb (± 2.8 g l^{-1}) and HbO_2 (± 1 g l^{-1}) and blood SO_2 ($\pm 4.1\%$) could be obtained and used as a benchmark against which the photoacoustically determined values could be compared.

5.3. Analysis of the measured photoacoustic waveforms

In principle, the forward model can be fitted to the entire time record of the detected photoacoustic signals for each wavelength. However, to minimize runtime, the amplitude of the detected signal was extracted at six discrete temporal points in the waveform for each wavelength and the forward model fitted to this reduced data set. This is illustrated in figure 5(a) which shows a typical detected photoacoustic signal. The temporal windows marked 1 to 3 correspond to the locations of the tubes whilst 4, 5 and 6 correspond to different depths within the extravascular space. Figure 5(b) shows an example of the amplitude as a function of wavelength for each of these temporal windows—this forms the measured spectroscopic data set to which the forward model is fitted.

Several features are notable in figure 5(b). The amplitudes of spectra 1 to 3, which correspond to the blood-filled tubes, decrease with increasing depth due to the optical attenuation in the intralipid. The latter contains mostly water, which is weakly absorbing across most of the near-infrared wavelength region except for the absorption peak around 975 nm. As a result, spectra 1 to 3 are significantly reduced between 900 nm and 1040 nm whilst spectra 4 and 5, which represent the photoacoustic signal amplitude from the extravascular space, are at a maximum in the same spectral region—the encoding of the water absorption peak on to the tube spectra is a clear example of the spatial-spectroscopic crosstalk issue referred to in section 2.

In making these measurements it was found that although the shape of spectrum 4 (which corresponds to the interface between the cuvette window and the extravascular space) agreed well with that predicted by the forward model, its amplitude was significantly lower (relative to the other spectra). Visual inspection suggested that this was due to the aggregation of the constituents of the extravascular space on the cuvette window producing a thin layer of increased optical attenuation. Since this layer constitutes an inhomogeneous region, the forward model is not strictly applicable because it assumes a homogeneous distribution of the optical coefficients in the extravascular space. To account for this, an additional scaling factor, k' was applied to spectrum 4. This in effect modifies K in equation (5) for the region close to window of the cuvette. k' was then included in the minimization process as an additional adjustable unknown parameter.

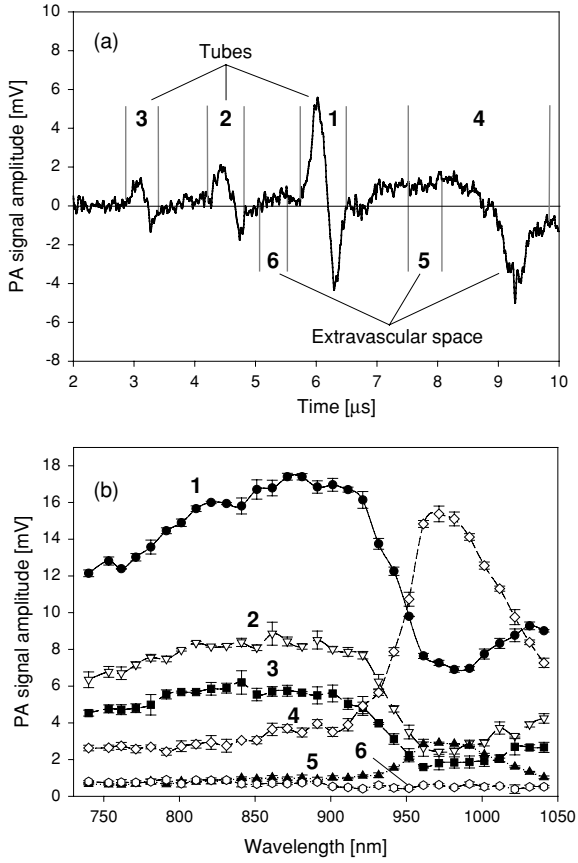

Figure 5. (a) Example of a detected photoacoustic waveform showing the six temporal windows from which the signal amplitude was extracted. Each window corresponds to a different distance z from the illuminated surface: **1**–tube 1 ($z = 4.4$ mm), **2**–tube 2 ($z = 6.7$ mm), **3**–tube 3 ($z = 8.8$ mm), **4**–extravascular ($z = 0$ mm), **5**–extravascular ($z = 1.8$ mm), **6**–extravascular ($z = 5.5$ mm). (b) Signal amplitude plotted as a function of wavelength for each temporal window. It is to this data set that the forward model is fitted. In this example, the blood SO_2 in the tubes was 93%.

5.3.1. Comparison of forward model output with measured photoacoustic spectra. Figure 6 shows the measured photoacoustic spectra for tube 1 for different concentrations of HbO_2 and HHb, achieved by varying the blood oxygenation saturation (SO_2) as described in section 5.2. A cursory inspection suggests that the photoacoustic spectra, and the way their shape changes with SO_2, are broadly similar to the well-known SO_2-dependent absorption spectra of blood—for example, the formation of the 760 nm peak as the blood becomes progressively more deoxygenated is clearly apparent.

However, as figure 6 shows, if we directly compare the measured photoacoustic spectra for the two extremes of almost fully oxygenated blood ($SO_2 = 99\%$) and almost fully deoxygenated blood ($SO_2 = 1.5\%$) against the known specific absorption spectra for HbO_2 and HHb, it is apparent that there are significant discrepancies. These differences are most apparent at wavelengths beyond 950 nm where the shape of the spectra is significantly distorted by the strong absorption due to the water in the extravascular space. Such spectral distortion will

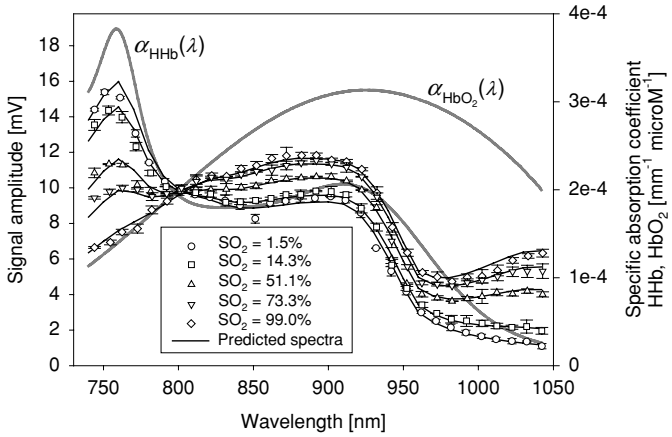

Figure 6. Comparison between measured photoacoustic spectra corresponding to tube 1 and the spectra predicted by the forward model (solid lines) for different blood SO_2 showing excellent agreement. The specific absorption coefficient spectra of oxyhaemoglobin, $\alpha_{HbO_2}(\lambda)$, and deoxyhaemoglobin, $\alpha_{HHb}(\lambda)$, are also shown for comparison.

compromise any attempt to recover the concentrations of HHb and HbO_2 by fitting their absorption spectra directly to the measured photoacoustic spectra, as a linear spectroscopic decomposition would seek to do. By contrast, the shapes of the spectra predicted by the forward model for these two extremes of blood SO_2 (and all the intermediate SO_2 values) are in excellent agreement with the measured data. As well as indicating the accuracy of the forward model, this again underscores the need to account for the influence of spectrally significant chromophores located outside the region of interest (in this case tube 1) if a spectroscopic-based analysis is to yield quantitatively accurate results.

6. Results

Photoacoustic signals were captured at different wavelengths for intravascular SO_2 values between 2% and 100% for three different extravascular space compositions: (i) intralipid only, (ii) intralipid and blood and (iii) intralipid, blood and the NIR dye. This provided the measured data set from which the concentrations of the chromophores in the intravascular and extravascular space were recovered using the inversion scheme. In section 6.1, the photoacoustically determined values of the intravascular HbO_2 and HHb concentrations are discussed. From these, the derived parameters of blood SO_2 and the total haemoglobin concentration were obtained and are presented in sections 6.2 and 6.3, respectively. The measurements of the extravascular concentrations of haemoglobin and the near-infrared dye are discussed in sections 6.4 and 6.5 and the values for the scattering coefficient in section 6.6.

6.1. Absolute concentrations of intravascular oxyhaemoglobin and deoxyhaemoglobin

Figure 7 shows the photoacoustically determined concentrations of oxyhaemoglobin and deoxyhaemoglobin, $c_{HbO_2 i}$ and $c_{HHb i}$, respectively, for each tube and extravascular space composition plotted against the values provided by the CO-oximeter—the uncertainty of the

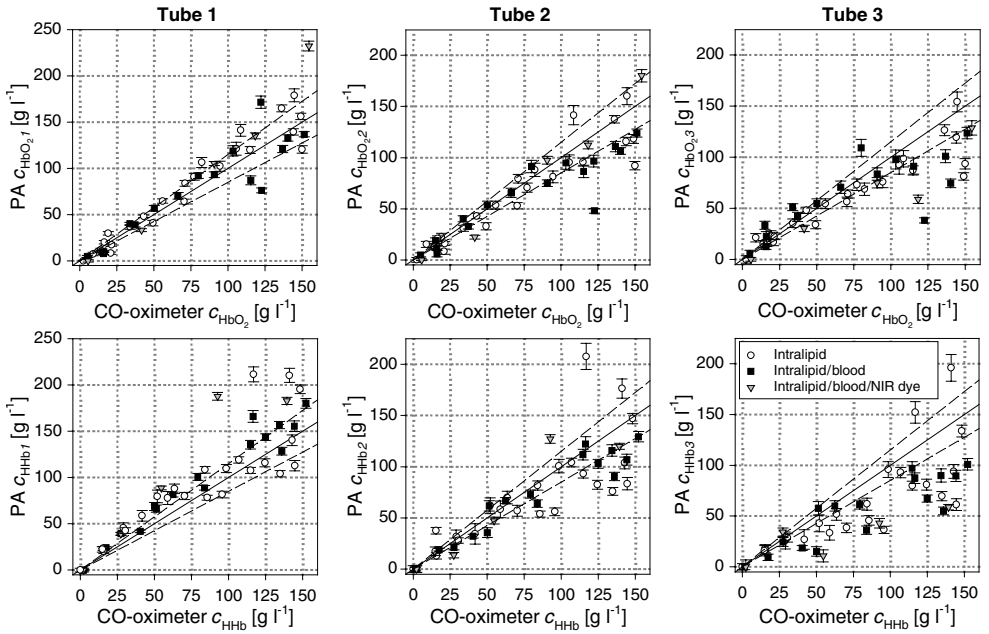

Figure 7. Photoacoustically determined intravascular oxyhaemoglobin concentration $c_{HbO_2 i}$ (top row) and deoxyhaemoglobin concentration $c_{HHb i}$ (bottom row) for tubes $i = 1$, 2 and 3 compared to the CO-oximeter measurements. The data are for the three different compositions of the extravascular space: (i) intralipid solution only, (ii) intralipid and blood and (iii) intralipid, blood and the NIR dye. The solid line indicates the line of unity and the dashed lines indicate a percentage error of 15%

Table 1. The accuracy and resolution of the photoacoustically determined intravascular oxyhaemoglobin and deoxyhaemoglobin concentrations, $c_{HbO_2 i}$ and $c_{HHb i}$ for each tube ($i = 1$, 2, 3) for different constituents of the extravascular space. By comparison, the uncertainty in the CO-oximeter measurements is ± 1.0 g l^{-1} for HbO_2 and ± 2.8 g l^{-1} for HHb.

		Accuracy (%)		Resolution (g l^{-1})	
	i	$c_{HbO_2 i}$	$c_{HHb i}$	$c_{HbO_2 i}$	$c_{HHb i}$
Intralipid	1	+5.2	+23.2	±3.3	±4.5
	2	−5.3	−7.1	±4.2	±5.6
	3	−10.1	−19.6	±4.9	±6.2
Intralipid/blood	1	−6.1	+21.9	±3.0	±3.4
	2	−13.8	−11.3	±3.8	±4.0
	3	−3.4	−33.6	±5.2	±4.7
Intralipid/blood/NIR dye	1	+15.2	+45.2	±2.7	±2.5
	2	+6.9	−10.1	±3.3	±3.4
	3	−27.8	−41.9	±4.2	±4.9

latter is ± 1.0 g l^{-1} for HbO_2 and ± 2.8 g l^{-1} for HHb. The accuracy and resolution of the measurements is provided in table 1.

Figure 7 shows that the majority of the photoacoustically determined values of $c_{HbO_2 i}$ and $c_{HHb i}$ are in broad agreement with the CO-oximeter values, the former increasing linearly with the latter and in reasonable quantitative agreement. The absolute error in the measurements

appears to scale with the concentration indicating an approximately constant percentage error—as figure 7 shows, most of the data for tubes 1 and 2 lie within a fixed percentage error of 15% (indicated by the dashed line) irrespective of concentration. This is less so for tube 3 as a consequence of a low signal-to-noise ratio (SNR) due to the greater depth at which it is located. An insight into the source of these errors can be gained by comparing the accuracy of the concentration values for each tube and extravascular space composition.

The accuracy is given by the mean of the percentage difference between the photoacoustically determined $c_{\mathrm{HbO}_2 i}$ and $c_{\mathrm{HHb}i}$ and the CO-oximeter values and is shown in table 1 for concentrations >10 g l^{-1}. Concentrations below this are comparable to the measurement resolution and therefore excluded. The nature and bias of the values in table 1 suggest specific limitations in the forward model. For example, $c_{\mathrm{HbO}_2 i}$ and $c_{\mathrm{HHb}i}$ tend to be overestimated for tube 1 while they are underestimated for tube 3. This is considered to be most likely due to limitations in the FE light transport model which assumes a two-dimensional geometry. As a consequence, the shape of the incident excitation beam is not circular as it is in reality but an infinitely long line of width equal to the beam diameter. This means that the absorbed optical energy density, and hence the photoacoustic signal amplitude, at greater depths is overestimated leading to an underestimation of the intravascular $c_{\mathrm{HbO}_2 i}$ and $c_{\mathrm{HHb}i}$ in tubes 2 and 3. Other model-based limitations that could produce similar scaling errors are the approximate nature of the corrections for the detector directivity and the attenuation described in section 3.2. One further observation is that the results for $c_{\mathrm{HHb}i}$ appear to be generally poorer than those for $c_{\mathrm{HbO}_2 i}$. This may be due to the lower average absorption by deoxyhaemoglobin across the detected wavelength range resulting in lower sensitivity to $c_{\mathrm{HHb}i}$.

The repeatability of the measurements in figure 7 is largely dependent upon experimental uncertainties, principally due to the acquisition of the data over a series of experiments rather than a single run. Thus, variations in the positioning of the tubes which had to be removed and realigned between each experiment are a possible source of error as is the dynamic nature of the extravascular space optical properties. For example, the repeatability appears to decrease when both blood and the NIR dye are added (individually or together) to the extravascular space. The need to continuously stir the intralipid solution in order to prevent the red blood cells from settling and replace the dye at frequent intervals due to its observed instability in aqueous solution made it difficult to ensure that the optical properties of the extravascular space remained truly constant both throughout the measurement period and between experimental runs.

The measurement resolution which is given by the mean of the error bar values for all the data obtained for a specific tube is comparable to that of the CO-oximeter with an average value (over all the data) of ± 3.9 g l^{-1} which corresponds to 60 μM. The resolution is dependent upon the SNR of the detected photoacoustic signals and therefore decreases with the increasing tube depth. Interestingly, the resolution in $c_{\mathrm{HbO}_2 i}$ and $c_{\mathrm{HHb}i}$ is slightly higher for measurements made on phantoms with additional extravascular chromophores, an indication of the tighter constraints on the inverse problem provided by the additional spectral characteristics introduced by these chromophores.

6.2. Intravascular blood oxygen saturation

Equation (9) was used to calculate the intravascular blood oxygen saturation (SO_2) from the photoacoustically determined values of $c_{\mathrm{HbO}_2 i}$ and $c_{\mathrm{HHb}i}$ presented in the previous section. Figure 8 shows the results for each of the three tubes compared to the blood SO_2 measured using the CO-oximeter. The accuracy and resolution (as defined in the previous section) of the measurements are given in table 2.

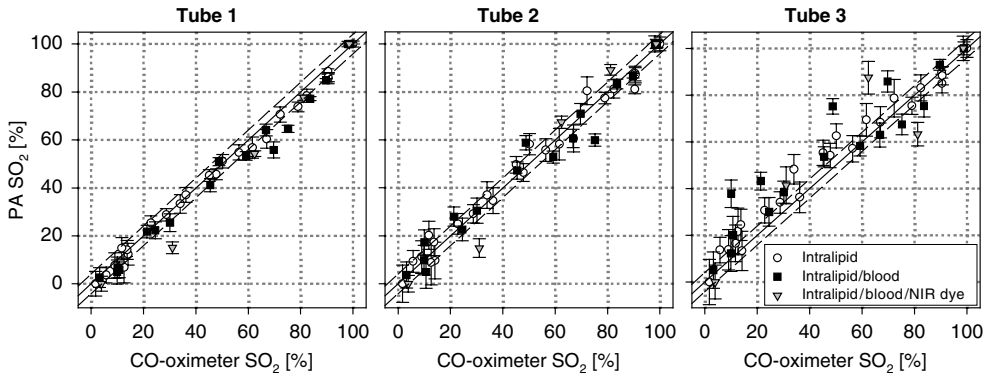

Figure 8. Photoacoustically determined intravascular blood oxygen saturation (SO_2) measurements compared to the CO-oximeter measurements for each tube and for the three different compositions of the extravascular space: (i) intralipid solution only, (ii) intralipid and blood and (iii) intralipid, blood and the NIR dye. The solid line is the line of unity and the dashed lines represent the uncertainty in the CO-oximeter measurements (±4.1% SO_2).

Table 2. The accuracy and resolution of the photoacoustically determined intravascular blood SO_2 measurements for each tube ($i = 1, 2, 3$) for different constituents of the extravascular space. The uncertainty in the CO-oximeter measurement is ±4.1% SO_2.

	i	Accuracy (%SO_2)	Resolution (%SO_2)
Intralipid	1	−1.8	±2.8
	2	0.0	±4.9
	3	+4.0	±6.1
Intralipid/blood	1	−3.7	±2.6
	2	−0.5	±3.8
	3	+7.0	±5.0
Intralipid/blood/NIR dye	1	−6.0	±1.6
	2	−1.1	±2.8
	3	+3.3	±6.5

Figure 8 shows that the results compare favourably with the CO-oximeter measurements. The photoacoustic SO_2 increases linearly with CO-oximeter SO_2 and is in good quantitative agreement for all oxygenations—for tubes 1 and 2, the measurements are generally within the uncertainty of the CO-oximeter (±4.1% SO_2). The data for tube 3 show larger deviations from the unity line, due to the increased depth, and hence the reduced SNR, in the detected photoacoustic signal.

It is noticeable from figure 8 that the SO_2 measurements are visually 'better' than those of the absolute chromophore concentrations in the previous section. The data are closer to the line of unity and with less scatter around it. This is related to the ability of the forward model to accurately predict both the shape and relative amplitude of the measured spectra. As figure 5(b) shows, the measured data comprises a total of six spectra: one for each tube and three for the extravascular space. To recover the absolute concentrations, the model output has to fit to all six measured spectra simultaneously. The model must therefore accurately describe not only the shape of each spectrum but correctly scale them relative to each other. If the latter, significantly more challenging requirement, is not fulfilled, for example because of the limitations of the model outlined in section 6.1, an error in the values

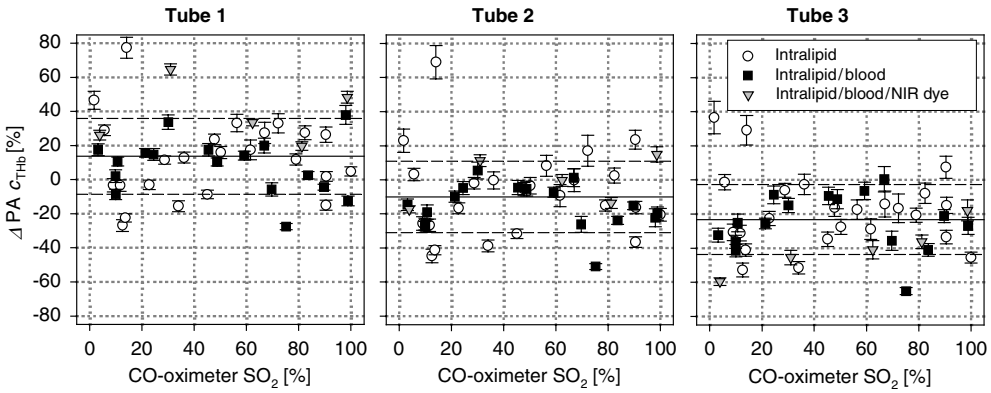

Figure 9. Plots of total intravascular haemoglobin concentration ΔPA c_{THbi} as a function of the intravascular blood SO_2. The solid line indicates the mean of all data while the dashed lines indicate the standard deviation. The accuracy of the c_{THb} measurements by the CO-oximeter was approximately ±2.0%.

of the absolute concentrations of HHb and HbO_2 returned by the inversion will be introduced. However this error will be the same for both HHb and HbO_2 and therefore cancel when SO_2 is calculated. The implication of this explanation is that the model accurately describes the shape of the measured photoacoustic spectra. This appears reasonable, evidenced by the excellent agreement between the measured and theoretical spectra for blood of different SO_2 shown in figure 6. More significant is the consistently high SO_2 measurement accuracy over the full SO_2 range as this is accompanied by very significant changes in the shape of the measured spectra—i.e., contrast the shape of the spectra for $SO_2 = 1.5\%$ to that for $SO_2 = 99\%$ in figure 6. The spectroscopic robustness of the forward model is further underscored by the fact that the measurement accuracy is largely unchanged by the introduction of blood and the NIR dye into the extravascular space, both of which impose very significant changes on the shape of the measured extravascular and intravascular spectra.

Despite the high accuracy, there are some systematic errors in $c_{HbO_2 i}$ and c_{HHbi} that appear to propagate through to the SO_2 measurements. SO_2 tends to be underestimated for tube 1 and overestimated for tube 3 suggesting there are some model-based limitations in accurately representing the shape of the measured spectra. For example, it was noted that the shape of a tube spectrum is affected by inaccuracies in the geometrical parameters of the tube. The need to approximate its cylindrical geometry by a square in the FE light transport model and the relatively coarse grid element size compared to the tube diameter are possible sources of error in this respect.

As with the concentration data, the resolution decreases with the increasing tube depth, due to the corresponding decrease in SNR. Also in common with the data in the previous section, the measurement resolution appears to be slightly higher for the measurements made on phantoms with the additional extravascular chromophores. The average value of the resolution (over all the data) is ±4% and thus comparable to that of the CO-oximeter (±4.1%).

6.3. Total intravascular haemoglobin concentration

The plots in figure 9 show the percentage difference, ΔPA c_{THbi}, between the photoacoustically determined total intravascular haemoglobin concentration, PA c_{THbi}, and that measured using

the CO-oximeter for all oxygenations studied. The calculation of the difference in per cent was necessary since the total haemoglobin concentration was different for each experiment.

ΔPA $c_{\mathrm{THb}i}$ was obtained using

$$\Delta\mathrm{PA}c_{\mathrm{THb}i} = \frac{\mathrm{PA}c_{\mathrm{THb}i}}{\mathrm{CO-oximeter}\, c_{\mathrm{THb}i}} \times 100\% - 100\%. \tag{12}$$

Figure 9 shows that there is a systematic error which begins as an overestimation for tube 1 (+13.7%) and changes into an underestimation for tube 2 (−10.1%) and tube 3 (−23.2%). As with the errors in the intravascular $c_{\mathrm{HbO}_2 i}$ or $c_{\mathrm{HHb}i}$ in section 6.1, this is considered to be a consequence of limitations in the forward model. In addition, figure 9 illustrates that the error in the determined intravascular $c_{\mathrm{THb}i}$ is largely independent of blood SO_2, further evidence of the spectroscopic accuracy and robustness of the forward model.

6.4. Total extravascular haemoglobin concentration

The inversion also yields the extravascular concentrations of oxyhaemoglobin and deoxyhaemoglobin, the sum of which provides the total extravascular haemoglobin concentration, $c_{\mathrm{THb}ev}$. For the measurements in which the extravascular space consisted of intralipid only, the inversion consistently gives $c_{\mathrm{THb}ev} = 0$ g l^{-1} with very good accuracy (<0.01 g l^{-1}). When blood was introduced into the extravascular space (with a total haemoglobin concentration typically in the range 3.7–4.1 g l^{-1}) to form the intralipid/blood or intralipid/blood/dye solutions, the inversion yielded an overestimation of $c_{\mathrm{THb}ev}$ of +1.0 g l^{-1} (equivalent to approximately +25%).

The determined extravascular concentrations are strongly dependent upon the accuracy with which the forward model scales the amplitude of the extravascular photoacoustic signal for different depths. A possible source of error arises from the assumption that the geometrical acoustic attenuation (due to the spreading of the wavefront) for the contributions corresponding to the extravascular space is proportional to $z_{\mathrm{d}}{}^{-2/3}$. This relationship is strictly only valid for the signal corresponding to the surface as it depends on the lateral extent of the illumination beam which varies with depth. A slight difference between the modelled and true attenuation could therefore result in the systematic overestimation or underestimation of the extravascular spectrum and hence the extravascular chromophore concentrations. This error would also impact on the accuracy of the determined intravascular chromophore concentrations.

The resolution was $\pm$0.2 g l^{-1} (equivalent to $\pm$3.1 μM) for all experiments, which was much higher than the resolution obtained for concentration measurements for the intravascular space (average $\pm$3.9 g l^{-1} which corresponds to $\pm$60 μM). This difference is due to the higher sensitivity of the photoacoustic spectra to extravascular chromophores, a consequence of the much greater pathlengths that the light travels through in the extravascular space compared to the intravascular space. For this reason, a change in the extravascular haemoglobin concentration leads to a much stronger change in the photoacoustic signal emitted by a tube than that produced by an identical change in the intravascular haemoglobin concentration.

6.5. Extravascular NIR dye concentration

For the measurements in which the near-infrared dye was added to the intralipid/blood suspension the mean photoacoustic c_{Dye} was determined as 9.9×10^{-4} g l^{-1}, which compares well with the true dye concentration of 10.8×10^{-4} g l^{-1} (1.7 μM). The accuracy in c_{Dye} is therefore -0.9×10^{-4} g l^{-1} or −8.3%. The resolution in c_{Dye} was calculated from the uncertainties in the measurements as $\pm0.39 \times 10^{-4}$ g l^{-1}, which is equivalent to $\pm$63 nM—

approximately a factor of 50 higher than for the extravascular haemoglobin due to the higher specific extinction coefficient of the dye.

6.6. Scattering coefficient

In addition to yielding chromophore concentrations, the inversion also provided k_{scat} from which μ_s can be obtained using equation (8) and therefore the reduced scattering coefficient $\mu_s' = (1-g)\mu_s$. To compare the values of μ_s' produced by the inversion, a photoacoustic signal was generated in a solution of pure intralipid at 975 nm. By fitting an exponential function to the compressive part of the detected waveforms, the effective attenuation coefficient, μ_{eff}, was determined (Laufer *et al* 2005). Since the μ_a of a 1.5% intralipid suspension at 975 nm is approximately that of water, μ_s' can be calculated using

$$\mu_s' = \frac{\mu_{\text{eff}}^2}{3\mu_a} - \mu_a. \tag{13}$$

With this method, the μ_s' of the phantom was determined as 1.3 $\text{mm}^{-1} \pm 0.3$ mm^{-1}. The mean value produced by the inversion algorithm was 1.0 mm^{-1} and is therefore in good agreement with this. The accuracy in μ_s' at 975 nm obtained from the analysis of all photoacoustic spectra was -0.3 mm^{-1}. The resolution in μ_s was calculated from the uncertainty in the determined values as ± 0.2 mm^{-1}.

7. Discussion and conclusions

A model-based inversion scheme for recovering spatially resolved tissue chromophore concentrations from spectroscopic photoacoustic signals has been developed and experimentally validated. This approach forms the basis of a general methodology that has broad application, not only for non-invasively mapping the distribution of physiological parameters such as blood oxygenation but identifying and quantifying the accumulation of targeted contrast agents used in molecular imaging. The conclusions drawn from this study in relation to the methodology, the quantitative accuracy and measurement resolution of the technique and its application to quantitative photoacoustic imaging are outlined below.

Methodology. Two key conclusions in relation to the methodology are drawn. First, that an accurate forward model that accounts for all the relevant physical mechanisms that underlie the measured photoacoustic spectra is essential. Key to this is explicitly accounting for both the light transport and its wavelength dependence over the entire illuminated tissue volume. To achieve this, the forward model must be capable of being formulated as a function of an arbitrary distribution of optical coefficients in order to represent the highly optically heterogeneous nature of tissues. Second, a simple linear decomposition in which the photoacoustic signal amplitude is assumed to be proportional to the absorption coefficient at the region of interest only is likely to be of questionable validity: it neither takes into account the influence of the spectral characteristics of the chromophores and scatterers distributed throughout the irradiated volume nor acknowledges the inherently nonlinear nature of the signal generation mechanism. This is demonstrated conclusively in the appendix where even the least challenging goal of quantifying SO_2 (rather than absolute concentrations) in a blood vessel lying close to the surface is seriously compromised. Although there may be some very limited situations in which it might be possible to obtain accurate measurements using a linear inversion, for example in homogeneous media or one in which the spectral characteristics of

the region of interest dominate all others, it is not clear whether there are any practical *in vivo* applications in which these special circumstances might occur.

Quantitative accuracy and resolution. Although the technique can be applied to any chromophore, specific emphasis was placed on determining the concentrations of the physiologically significant chromophores, HbO_2 and HHb and from these, the derived parameters of blood SO_2 and total haemoglobin concentration. The resolution of the concentration measurements and the accuracy and resolution of the SO_2 are comparable to that of the CO-oximeter. The recovered concentrations of HbO_2 and HHb are of lower accuracy, principally due to the use of a 2D model to describe the 3D nature of light transport in tissue and the approximations involved in accounting for the acoustic attenuation due to the geometrical spreading of the wavefront. There is scope to address this by extending the light transport and acoustic propagation models to 3D through the use of efficient FE implementations (Arridge *et al* 1993, Schweiger and Arridge 1998) for the former and fast *k*-space acoustic propagation models for the latter (Cox and Beard 2005).

The resolution of the technique indicates that it should be possible to measure localized haemoglobin concentration changes, such as those within a blood vessel, in the tens of micromolar range. If, instead of being localized within a vessel, the haemoglobin can be viewed as being spatially distributed (as the capillary bed might be regarded) over the whole illuminated volume, micromolar resolutions are possible. As well as quantifying naturally occurring chromophores such as haemoglobin, this technique could be used to quantify endogenous chromophores such as an externally administered targeted contrast agent (or multiple contrast agents) designed to selectively accumulate at the site of a specific cellular receptor. From the data presented in this paper it is possible to estimate the likely detection sensitivity that can achieved using a typical NIR contrast agent such as indo-cyanine green (ICG), which has been used for photoacoustic molecular imaging (Kruger *et al* 2003, Xie *et al* 2006). Given that this has a specific extinction coefficients around 50 times higher than that of haemoglobin, it is estimated, from the intravascular haemoglobin concentration resolution (section 6.1), that it should be possible to detect localized accumulations of the order of 1 micromolar decreasing to tens of nanomolar if the contrast agent is spatially distributed over the whole illuminated volume.

Application to multiwavelength photoacoustic imaging. The ability to obtain a depth profile of chromophore concentrations by recording the photoacoustic signal detected at a single point has been demonstrated. Although useful in its own right, in that it demonstrates the quantitative, spatially resolved nature of the technique, its value is primarily as an intermediate step to achieving the eventual goal of recovering 2D or 3D maps of chromophore concentrations. This would be achieved by recording photoacoustic signals over a line or surface at multiple wavelengths and from these reconstructing 2D or 3D absorbed energy images at each wavelength using an acoustic backpropagation algorithm. There are then two possible approaches to recovering the concentrations from these images. The first is to simply increase the dimensionality of the inversion scheme described in this paper—that is to say, apply it to the reconstructed 2D or 3D multiwavelength absorbed energy images instead of a single-point multiwavelength time-domain signal—note that the backpropagation algorithm accounts for the acoustic propagation so the forward model would now comprise the FE light transport model alone. 2D or 3D absorbed energy images would overcome the main limitation of single-point measurements, which lies in the lack of information they provide about the spatial distribution of chromophores outside the field of view of the detector. Multidimensional images will provide the necessary geometric information to enable accurate modelling of the light transport over the entire illuminated volume, which will in turn make the described

method more generally applicable. The second, and more efficient approach, is to first fit the FE light transport forward model to each absorbed energy map (a fast recursive method for this is described in Cox *et al* (2005, 2006a, 2006b), to recover an image of μ_a for each wavelength and then apply a standard linear spectroscopic decomposition pixel by pixel. As well as providing images as opposed to a depth profile, increasing the dimensionality can be expected to provide higher accuracy as it avoids the approximations made in the current formulation of the forward model. For example if 3D absorbed energy maps are reconstructed, the 3D nature of acoustic propagation, and thus the geometrical acoustic attenuation factor, is implicitly accounted for in the reconstruction algorithm. The correction factors described in section 3.2, which are required when the photoacoustic signal is obtained at only a single spatial point, are therefore not required. Additionally, the FE light transport model that is fitted to the absorbed energy maps can be formulated in 3D thus avoiding the limitations of describing the light transport in 2D.

In summary, quantitative spectroscopic photoacoustic techniques offer a uniquely powerful investigative tool for non-invasively measuring absolute chromophore concentrations. The key distinguishing feature of this technique, in contrast to other optical spectroscopic methods, is the high spatial resolution it can provide—tens of microns for mm penetration depths to mm for cm penetration depths. Ultimately, by combining the methodology outlined in this paper with photoacoustic imaging techniques, it offers the prospect of being able to obtain 3D images of the concentrations of endogenous tissue chromophores such as oxyhaemoglobin and deoxyhaemoglobin in order to map absolute oxygen saturation over the microvasculature. This would have many applications both in clinical medicine and basic research. These include studying oxygenation heterogeneity in tumours and other tissue pathologies and responses characterized by changes in oxygenation status such as soft tissue damage including burns, wounds and ulceration. Of equal importance is the potential to apply these methods to detecting and quantifying the accumulation of targeted contrast agents used in photoacoustic molecular imaging. This offers a wealth of opportunities, both in basic research for providing insight into the molecular processes that underlie disease and in the discovery of new drugs and other therapies.

Acknowledgment

This work is funded by the UK EPSRC.

Appendix. Analysis using a simple linear spectroscopic inversion

As discussed in section 1, it has previously been suggested that a simple linear spectroscopic decomposition could be used to recover chromophore concentrations, or derived parameters such as blood SO_2. This assumes that the photoacoustic signal amplitude is directly proportional to the total absorption coefficient μ_a at a point which is given by the sum of the absorption contributions by each chromophore at that point. Each contribution is linearly dependent upon the product of the chromophore concentration and its specific absorption spectrum—in other words an expression similar to that of equation (6) would form the forward model for the photoacoustic spectra corresponding to the intravascular space. The appeal of this approach is its mathematical simplicity and low computational cost as the forward model can be written as a set of simultaneous linear equations and efficiently inverted using well-established matrix inversion methods. Appealing as this approach is, it is of questionable validity. First, the photoacoustic signal amplitude is proportional to the local absorbed energy

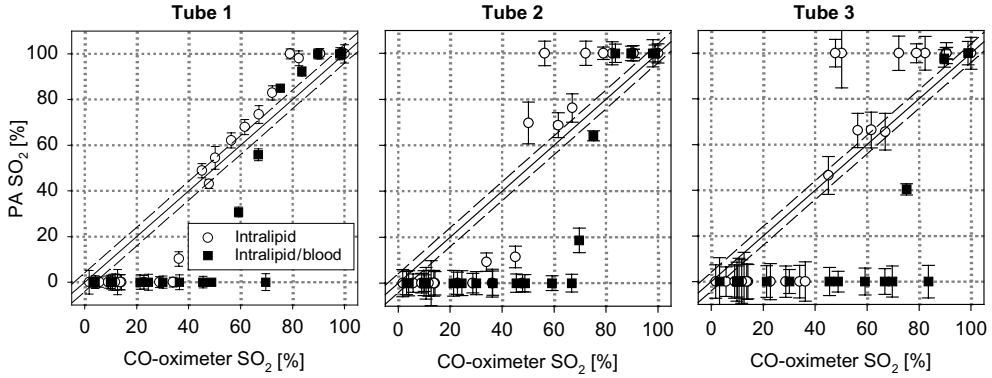

Figure 10. Photoacoustically determined intravascular SO_2 compared to the CO-oximeter measurements for each tube (with and without blood in the extravascular space) using a standard linear spectroscopic decomposition. Compare these measurements to those in figure 8 which were recovered from the same measured photoacoustic spectra but using the nonlinear inversion scheme.

which is given by the product of the local μ_a and the fluence. It is not therefore strictly a linear function in μ_a, although there is evidence to suggest that under certain conditions such as a homogeneous target (Laufer *et al* 2005) and for a limited range of μ_a (Maslov *et al* 2006), the nonlinearity is small. Second, and more importantly, a simple linear model does not account for the spectral characteristics of the chromophores and scatterers located outside the region from which the photoacoustic signal originates. For example, as shown in section 5.3, the wavelength dependence of the photoacoustic signal in the tubes is encoded with the spectral characteristics of the extravascular space. In essence, the measured photoacoustic spectra are corrupted and attempting to fit the simple linear model is unlikely to yield quantitatively accurate results.

This is illustrated by the results in figure 10 which were obtained by reanalysing the measured photoacoustic spectra obtained in this study using a simple linear spectroscopic inversion (details of the algorithm used are given in section 5.1.2 in Laufer *et al* (2005)). Note that we attempt the less challenging goal of inverting for intravascular SO_2 rather than absolute concentrations of HHb and HbO_2 which are much more sensitive to model-based errors. Initially, the linear model was fitted to the entire wavelength range of the measured photoacoustic spectrum (740 nm–1040 nm). This resulted in very poor agreement between the measured and fitted spectra largely because the linear model does not account for the reduction in the photoacoustic signal amplitude around 975 nm due to the strong absorption by the water in the extravascular space. The analysis was therefore repeated for the wavelength range of 740 nm to 900 nm, where the effect of water absorption on the photoacoustic spectra is reduced. The blood SO_2 determined this way is shown in figure 10 as a function of the CO-oximeter SO_2 for measurements on phantoms with and without extravascular blood.

The agreement of the photoacoustic blood SO_2 with the CO-oximeter measurements is generally poor. The only possible exception is for SO_2 between 50% and 80% for tube 1 and then only provided there is no blood in the extravascular space. At other blood SO_2 levels, greater depths and especially in the presence of extravascular blood, the linear model tends to calculate extreme blood SO_2 values of either 0% or 100% irrespective of the true blood SO_2. Finally it is noted that when attempting to recover the absolute HHb and HbO_2 concentrations, the results were nonsensical with randomly distributed discrepancies at least an order of magnitude from the true values.

Although these results highlight the limitations of a simple linear spectroscopic decomposition, it is instructive to consider whether there are any circumstances under which it could conceivably work *in vivo*. For example, the results in figure 10 suggest that it might in the case of a superficial blood vessel surrounded by tissue composed of chromophores of either uniform spectral characteristics or relatively weakly absorbing or both. However, it is difficult to envisage such a fortuitous set of circumstances ever occurring. The spectral contribution of HHb and HbO_2 in the capillary bed will almost always be significant, even if that due to other tissue chromophores such as lipids, water and melanin can be minimized by appropriate choice of the wavelength range.

References

Arridge S R, Schweiger M, Hiraoka M and Delpy D T 1993 A finite-element approach for modeling photon transport in tissue *Med. Phys.* **20** 299–309

Beard P C 2003 Interrogation of free-space Fabry-Perot sensing interferometers by angle tuning *Meas. Sci. Technol.* **14** 1998–2005

Beard P C, Perennes F and Mills T N 1999 Transduction mechanisms of the Fabry-Perot polymer film sensing concept for wideband ultrasound detection *IEEE Trans. Ultrason. Ferroelectr. Freq. Control* **46** 1575–82

Cope M 1991 The application of near infrared spectroscopy to non invasive monitoring of cerebral oxygenation in the newborn infant *PhD Thesis* University College London

Cox B T, Arridge S R and Beard P C 2006a Quantitative photoacoustic image reconstruction for molecular imaging 2006 *Proc. SPIE* **6086** 60861M-1–9

Cox B T, Arridge S R, Köstli K P and Beard P C 2005 Quantitative photoacoustic imaging: fitting a model of light transport to the initial pressure distribution *Proc. SPIE* **5697** 49–55

Cox B T, Arridge S R, Köstli K P and Beard P C 2006b 2D quantitative photoacoustic image reconstruction of absorption distributions in scattering media using a simple iterative method *Appl. Opt.* **45** 1866–74

Cox B T and Beard P C 2005 Fast calculation of pulsed photoacoustic fields in fluids using k-space methods *J. Acoust. Soc. Am.* **117** 3616–27

Esenaliev R O, Larina I V, Larin K V, Deyo D J, Motamedi M and Prough D S 2002 Optoacoustic technique for noninvasive monitoring of blood oxygenation: a feasibility study *Appl. Opt.* **41** 4722–31

Fainchtein R, Stoyanov B J, Murphy J C, Wilson D A and Hanley D F 2000 Local determination of hemoglobin concentration and degree of oxygenation in tissue by pulsed photoacoustic spectroscopy *Proc. SPIE* **3916** 19–33

Hale G M and Querry M R 1973 Optical constants of water in 200 nm to 200 μm wavelength region *Appl. Opt.* **12** 555–63

Kolkman R G M, Hondebrink E, Steenbergen W and de Mul F F M 2003 *In vivo* photoacoustic imaging of blood vessels using an extreme-narrow aperture sensor *IEEE J. Sel. Top. Quantum Electron.* **9** 343–6

Köstli K P and Beard P C 2003 Two-dimensional photoacoustic imaging by use of Fourier-transform image reconstruction and a detector with an anisotropic response *Appl. Opt.* **42** 1899–908

Kruger R A, Kiser W L, Reinecke D R, Kruger G A and Miller K D 2003 Thermoacoustic molecular imaging of small animals *Mol. Imaging* **2** 113–23

Landau L D and Lifshitz E M 1987 *Fluid Mechanics* 2nd edn (Oxford: Heinemann)

Laufer J, Elwell C, Delpy D and Beard P 2004 Pulsed near-infrared photoacoustic spectroscopy of blood *Proc. SPIE* **5320** 57–68

Laufer J, Elwell C, Delpy D and Beard P 2005 *In vitro* measurements of absolute blood oxygen saturation using pulsed near-infrared photoacoustic spectroscopy: accuracy and resolution *Phys. Med. Biol.* **50** 4409–28

Laufer J, Elwell C, Delpy D and Beard P 2006a Absolute measurements of local chromophore concentrations using pulsed photoacoustic spectroscopy *Proc. SPIE* **6086** 60861J-1–8

Laufer J, Elwell C, Delpy D and Beard P 2006b Spatially resolved blood oxygenation measurements using time-resolved photoacoustic spectroscopy *Oxygen Transport to Tissue XXVII* pp 155–60 (*Advances in Experimental Medicine and Biology* vol 578)

Maslov K, Sivaramakrishnan M, Zhang H F, Stoica G and Wang L V 2006 Technical considerations in quantitative blood oxygenation measurement using photoacoustic microscopy *in vivo Proc. SPIE* **6086** 60860R-1–11

Niederhauser J J, Jaeger M, Lemor R, Weber P and Frenz M 2005 Combined ultrasound and optoacoustic system for real time high contrast vascular imaging in vivo *IEEE Trans. Med. Imaging* **24** 436–40

Oh J T, Li M L, Zhang H F, Maslov K, Stoica G and Wang L V 2006 Three-dimensional imaging of skin melanoma in vivo by dual-wavelength photoacoustic microscopy *J. Biomed. Opt.* **11** 034032-1–4

Oraevsky A A, Savateeva E V, Solomatin S V, Karabutov A, Andreev V G, Gatalica Z, Khamapirad T and Henrichs P M 2002 Optoacoustic imaging of blood for visualization and diagnostics of breast cancer *Proc. SPIE* **4618** 81–94

Paltauf G, Köstli K P, Frauchiger D and Frenz M 2001 Spectral optoacoustic imaging using a scanning transducer *Hybrid Novel Imaging New Opt. Instrum. Biomed. Appl.* **4434** 81–8

Paltauf G, Schmidt-Kloiber H and Guss H 1996 Light distribution measurements in absorbing materials by optical detection of laser-induced stress waves *Appl. Phys. Lett.* **69** 1526–8

Savateeva E V, Karabutov A A, Solomatin S V and Oraevsky A A 2002 Optical properties of blood at various levels of oxygenation studied by time resolved detection of laser-induced pressure profiles *Proc. SPIE* **4618** 63–75

Schweiger M and Arridge S R 1998 Comparison of two- and three-dimensional reconstruction methods in optical tomography *Appl. Opt.* **37** 7419–28

Simpson R, Laufer J, Kohl M, Essenpreis M and Cope M 1997 Near infrared optical properties of *ex vivo* human skin and sub-cutaneous tissues using reflectance and transmittance measurements *Proc. SPIE* **2979** 307–13

Stantz K M, Liu B, Cao M, Reinecke D, Miller K and Kruger R 2006 Photoacoustic spectroscopic imaging of intra-tumor heterogeneity and molecular identification *Proc. SPIE* **6086** 608605-1–11

Troy T A, Page D L and Sevic-Mucraca E M 1996 Optical properties of normal and diseased breast tissues: prognosis for optical mammography *J. Biomed. Opt.* **1** 342–55

van Staveren H J, Moes C J M, van Marle J, Prahl S A and van Gemert M J C 1991 Light-scattering in intralipid 10% in the wavelength range of 400–1100 nm *Appl. Opt.* **30** 4507–14

van Veen R L P, Sterenborg H J C M, Pifferi A, Torricelli A, Chikoidze E and Cubeddu R 2005 Determination of visible near-IR absorption coefficients of mammalian fat using time- and spatially resolved diffuse reflectance and transmission spectroscopy *J. Biomed. Opt.* **10** 054004-1–6

Wang X, Xie X, Ku G and Wang L V 2006 Noninvasive imaging of hemoglobin concentration and oxygenation in the rat brain using high-resolution photoacoustic imaging *J. Biomed. Opt.* **11** 024015-1–9

Wang X D, Ku G, Xie X Y, Wang Y W, Stoica G and Wang L V 2004 Non-invasive functional photoacoustic tomography of blood oxygen saturation in the brain *Proc. SPIE* **5320** 69–76

Wang X D, Pang Y J, Ku G, Xie X Y, Stoica G and Wang L H V 2003 Noninvasive laser-induced photoacoustic tomography for structural and functional *in vivo* imaging of the brain *Nat. Biotechnol.* **21** 803–6

Wray S, Cope M, Delpy D T, Wyatt J S and Reynolds E O R 1988 Characterisation of the near-infrared absorption spectra of cytochrome-AA3 and haemoglobin for the non-invasive monitoring of cerebral oxygenation *Biochim. Biophys. Acta* **933** 184–92

Xie X, Li M-L, Oh J-T, Ku G, Wang C, Li C, Similache S, Lungu G F, Stoica G and Wang L V 2006 Photoacoustic molecular imaging of small animals *in vivo Proc. SPIE* **6086** 608606-1–6

Zhang E Z and Beard P C 2006 2D backward-mode photoacoustic imaging system for NIR (650–1200 nm) spectroscopic biomedical applications *Proc. SPIE* **6086** 60860H-1–7